We are IntechOpen,
the world's leading publisher of
Open Access books
Built by scientists, for scientists

6,900
Open access books available

185,000
International authors and editors

200M
Downloads

Our authors are among the

154
Countries delivered to

TOP 1%
most cited scientists

12.2%
Contributors from top 500 universities

BOOK CITATION INDEX

CLARIVATE ANALYTICS

INDEXED

WEB OF SCIENCE™

Selection of our books indexed in the Book Citation Index
in Web of Science™ Core Collection (BKCI)

Interested in publishing with us?
Contact book.department@intechopen.com

Innovative Exploitation of Grating-Coupled Surface Plasmon Resonance for Sensing

G. Ruffato, G. Zacco and F. Romanato

Additional information is available at the end of the chapter

http://dx.doi.org/10.5772/51044

1. Introduction

Surface Plasmon Polaritons (SPPs) are confined solutions of Maxwell's equations which propagate at the interface between a metal and a dielectric medium and have origin from the coupling of the electromagnetic field with electron-plasma density oscillations inside the metal [1]. SPPs are localized in the direction perpendicular to the interface: field intensity decays exponentially from the surface with an extension length of the same order of the wavelength inside the dielectric and almost one order shorter in the metal [2]. These features make SPPs extremely sensitive to optical and geometrical properties of the supporting interface, such as shape, roughness and refractive indices of the facing media. Since these modes have a non-radiative nature, the excitation by means of a wave illuminating the metallic surface is possible only in the configurations providing the wavevector-matching between the incident light and SPP dispersion law (Surface Plasmon Resonance – SPR, see Figure 1). Prism-Coupling SPR (PCSPR) exploits a prism in order to properly increase incident light momentum and achieve SPP excitation, however this setup suffers from cumbersome prism alignment and it is not suitable for miniaturization and integration. A more amenable and cheaper solution consists in Grating-Coupling SPR (GCSPR), where the metal surface is modulated with a periodic corrugation. The plasmonic behaviour of these modulated metallic surfaces had been discovered since the early years of the last century by R.W. Wood [3] and the connection between Wood's anomalies and surface plasmons was finally established by J.J. Cowan and E.T. Arakawa [4]. A plane-wave illuminating the patterned area is diffracted by the periodic structure and it is possible for at least one of the diffracted orders to couple with SPP modes.

SPR has known an increasing interest in the design and realization of miniaturized label-free sensing devices based on plasmonic platforms. Surface plasmon modes in fact are extremely sensitive to changes in the refractive index of the facing dielectric medium: a thin coating

film or the flowing of a liquid solution alter SPP dispersion curve and cause resonance conditions to change (Figure 2). Thus it is possible to detect refractive index variations by simply analyzing the resonance shift: it is the basis of modern SPR-sensing devices [5]. SPR reveals itself as a useful instrument for the study of surface optical properties and it is a highly suitable candidate as application with sensing purposes in a large variety of fields: environmental protection, biotechnology, medical diagnostics, drug screening, food safety and security.
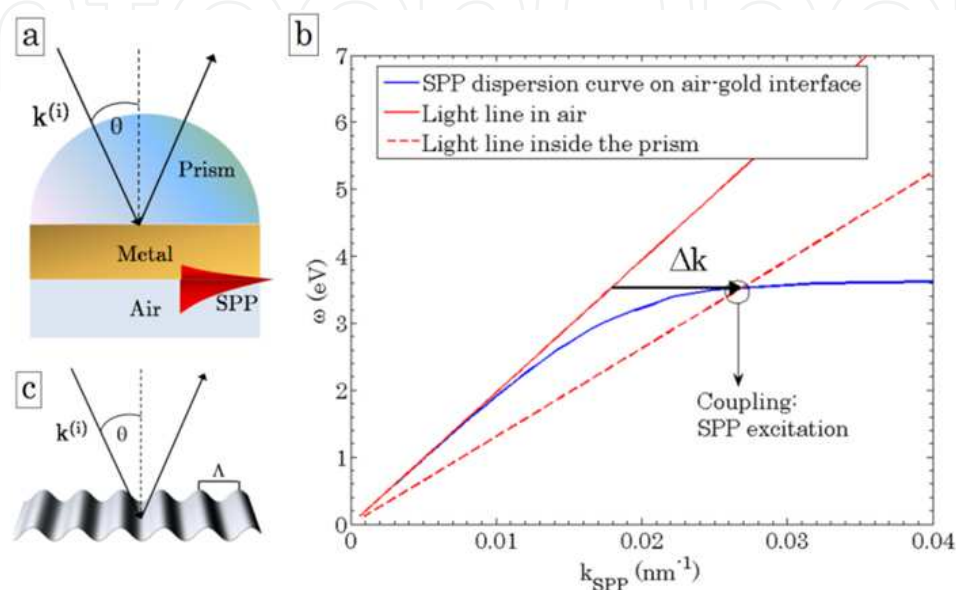

Figure 1. a) Kretschmann SPR configuration. b) SPP excitation with Prism-Coupling. The same effect of momentum-supply can be achieved by corrugating the metallic surface in the so-called Grating-Coupled SPR (c).

Currently, several groups are using different SPR approaches to detect the change of refractive index. Sensors using Prism-Coupled SPR (PCSPR) with Kretschmann configuration [6] can be readily combined with any type of interrogation: angular, wavelength, intensity or phase modulation [7]. PCSPR typically show refractive index sensitivity for angular interrogation architecture that ranges between 50-150°/RIU [8], with higher sensitivity at shorter wavelengths [9], and refractive index resolutions in the orders 10^{-6}-10^{-7} Refractive Index Units (RIU). However, PCSPR sensors suffer from cumbersome optical alignment and are not amenable to miniaturization and integration [10].

Grating-Coupled SPR (GCSPR) sensors instead, with either wavelength or angular interrogation, have been demonstrated to have sensitivity 2-3 times lower than PCSPR [11]. However, GCSPR has the intrinsic possibility to be used with different sensing architectures and interrogation systems. A parallel SPR angular detection was shown by Unfrict et al. to have the possibility for multi-detection for proteomic multi-array [12]. Homola's group demonstrated how a miniaturized GCSPR sensor implemented with a CCD allowed detection sensitivity of 50°/RIU and resolution of $5 \cdot 10^{-6}$ over 200 sensing parallel channels [13]. Alleyne has exploited the generation of an optical band gap by using prism-coupled to achieve sensitivity up to 680°/RIU by bandgap-assisted GCSPR [14]. A recent approach was

reported by Telezhnikova and Homola [15] with the development of a sensor based on spectroscopy of SPPs down to $5 \cdot 10^{-7}$ RIU. The strong compatibility of gratings with mass production makes SPP couplers extremely attractive for fabrication of low-cost SPR platforms .
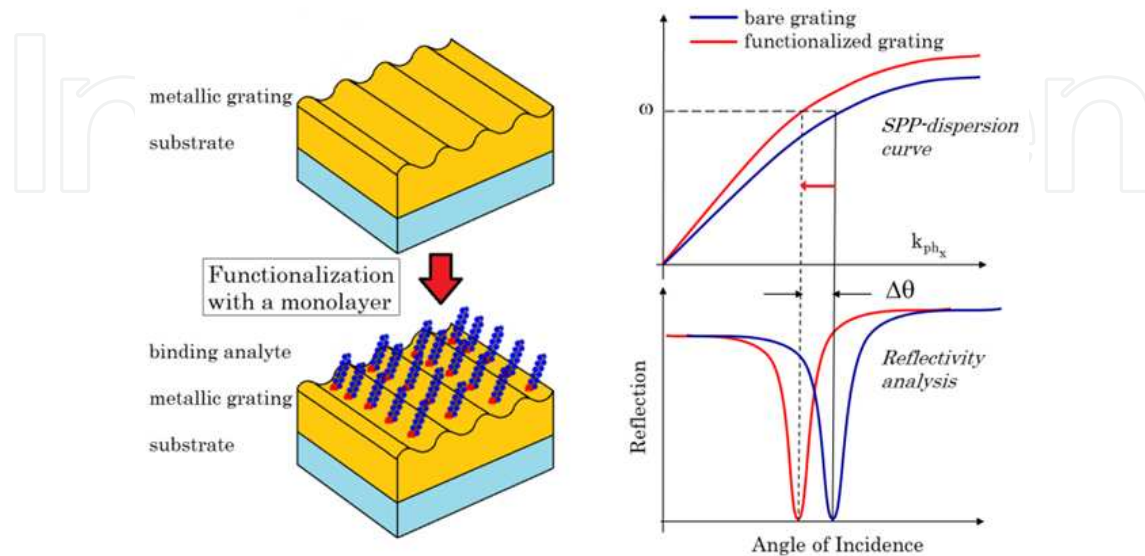
Figure 2. Surface Plasmon Resonance for sensing: the deposition of the analyte on the SPP-supporting surface results in a change of the dispersion curve and a consequent shift of the resonance dip.

Recently we have experimentally and theoretically described the effects of grating azimuthal rotation on surface plasmon excitation and propagation. More SPPs can be supported with the same illuminating wavelength [16] and sensitivity up to 1000°/RIU is achievable for the second dip in angular interrogation [17], which is one order of magnitude greater than that in a conventional configuration. On the top of that, the symmetry breaking after grating rotation makes polarization have a fundamental role on surface plasmon polaritons excitation [18] and the incident polarization must be properly tuned in order to optimize the coupling strength. This result leads to the possibility of exploiting the dependence of the optimal polarization on the resonance conditions, in order to design an innovative GCSPR configuration based on polarization interrogation in the conical mounting.

2. Nanofabrication of plasmonic gratings

2.1. Interferential lithography

Interferential Lithography (IL) is the preferred method for the fabrication of periodic patterns that must be spatially coherent over large areas [19]. It is a conceptually simple process where two coherent beams interfere in order to produce a standing wave which can be recorded over a sensitive substrate. The spatial period of the pattern can be as low as half the wavelength of the interfering light, allowing for structures down to about 100 nm using UV radiation. In Lloyd's Mirror Interferometer, one source is replaced by a mirror. Lloyd's mirror is rigidly fixed perpendicular to the surface and used to reflect a portion of incident

wavefront back to the other half. The angle of interference and thus the grating periodicity are set just by rotating the mirror/substrate assembly around the point of intersection between the mirror and the substrate. Simple trigonometry guarantees that the light reflected off the mirror is always incident at the same angle as the original beam. Moreover since the mirror is in a rigid connection with the wafer chuck, vibration of the setup or wandering of the incoming beam do not affect the exposure: this results in a more stable configuration and prevents the need of phase locking systems. Furthermore, it allows to change and control the grating period without any alignment or critical adjustment between two different sources and thus the system is very convenient to calibrate and tune.

The basic principles in order to record a pattern of desired period and amplitude are the following:

- *Grating period*: the incident beam angle has to be properly adjusted in order to obtain the desired periodicity according to the following law:

$$\Lambda = \frac{\lambda}{2\sin\theta} \tag{1}$$

where Λ is the resulting spatial periodicity of the grating, λ the beam wavelength and θ the incident beam angle (see Figure 3).

- *Grating amplitude*: amplitude is controlled by varying the exposure dose. Keeping fixed the beam intensity the exposure dose can be varied by changing the exposure time. The higher the dose on the resist, the higher the amplitude that is obtained after resist development.

In our system a 50 mW Helium-Cadmium (HeCd) laser emitting TEM00 single mode at 325 nm was used as light source. After a 2 m long free-space propagation, the expanded laser beam illuminates both the sample and the perpendicular mirror. The designed sample holder offers translational and rotational degrees of freedom, while a rigid mechanical connection between the mirror and the sample-chuck prevents phase distortion. The possibility to translate the sample stage in two directions allows a fine positioning of the system in the zone where the Gaussian beam distribution reaches its maximum and the best conditions in terms of beam intensity, uniformity and spatial coherence are achieved. On the other hand the sample stage rotation around vertical axis, with 8 mrad resolution, allows a fine setting of fringes periodicity.

Metallic gratings can be processed through a sequence of steps [20]: resist spinning, IL exposure, resist devolment, master replication, methal evaporation over the replica. Exposures can be performed over silicon samples of 2 x 2 cm² surface area. Silicon wafers have to be cleaned and pre-baked for 25 minutes at 120°C. A bottom anti-reflection layer can be also spun by spin coating in order to improve the exposure quality. Thus, a 120 nm thick film of photoresist S1805 (Microposit, Shipley European Limited, U.K.) and Propylene glycol monomethyl ether-1,2-acetate (PGMEA) solution (ratio 2:3) can be spun at the spinning rate of 3000 RPM for 30 seconds. After the exposure, a developing solution of MICROPOSIT MF-321 or MF-319 can be used.
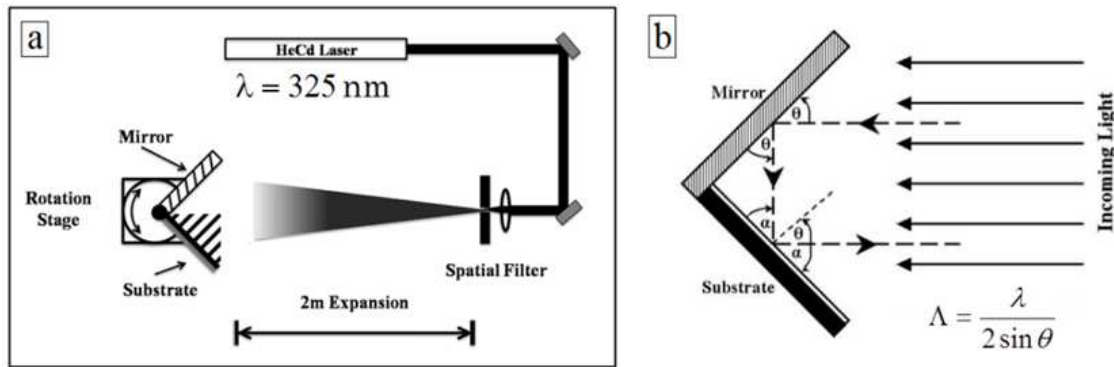
Figure 3. a) Scheme of the experimental IL setup. b) Detail of the sample holder configuration during the exposure.
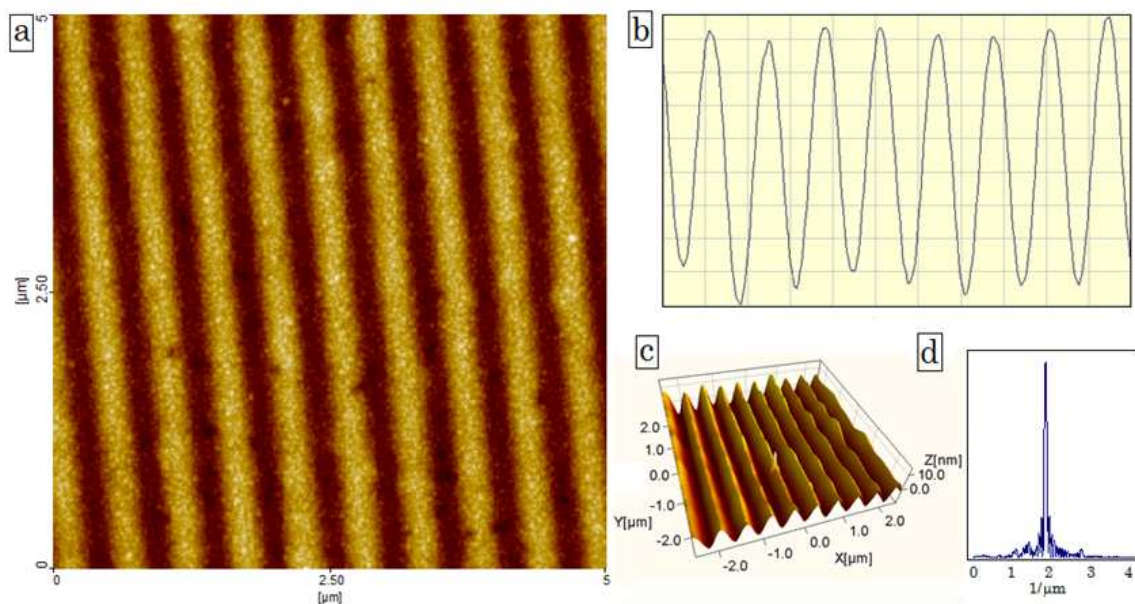
Figure 4. AFM analysis of a gold sinusoidal grating fabricated by interferential lithography of resist S1805 (period 505 nm, amplitude ~30 nm): top view (a), profile along the grating vector direction (b), 3D reconstruction (c), Fourier transform (d).

After the exposed resist has been developed, the result is a photonic crystal: a dielectric periodic surface which has no plasmonic feature yet. In order to realize a plasmonic crystal, the dielectric grating must be coated with a metallic layer of proper thickness, usually noble metals (silver or gold), for example by thermal evaporation. Common recipes consists in a silver layer with optimized thickness coated by a gold layer in order to prevent oxidation, or as an alternative an optimized gold layer over an adhesion layer of chrumium.

2.2. Soft-lithography replica

Soft-lithography is a useful technique in order to replicate pre-fabricated patterns with a nanometric resolution. It consists in making at first the negative replica of a pattern master onto a siliconic polymer and then in imprinting this pattern onto a photopolymeric substrate that cures when exposed to UV light.

In principle, a plasmonic grating could be obtained, as explained in the previous section, by simply coating a developed resist surface with specific noble metals, such as silver and gold over few nanometers of chromium or titanium as adhesion layers. However, many bio-molecular surface functionalization methods involve the use of organic solvents that may attack the photoresist pattern. To avoid this problem, a replica molding approach can be adopted in order to produce thiolene copies of the gratings [21]. Commercial thiolene resin (Norland Optical Adhesive – NOA61 [22]) can be chosen in order to exploit its relatively good resistance to organic solvents.

Resist patterns are usually replicated onto the thiolene resist film supported on microscope glass slides using polydimethylsiloxane (PDMS) molds. The latter are obtained by replicating the resist grating masters using RTV615 silicone. Base and catalyst of the two component silicone are mixed 10:1 ratio and degassed under vacuum. The PDMS is then cast against the resin masters and cured at 60°C, well below the resist post-exposure bake temperature (115° C) in order to prevent the resist pattern from distortion and after 2 hours the PDMS is peeled off from the resist master.

In order to obtain rigid and stable supports, the PDMS molds are bound to glass slides by exposing the flat backside of the PDMS mold and the glass slide to oxygen plasma before contacting them. The PDMS mold is then used to UV imprint the initial pattern onto a drop of NOA61 resin dripped on top of a glass slide by just slightly pressing the mold onto the liquid resin and exposing it to the UV light (365 nm) of a Hg vapor flood lamp at the proper distance and for enough time. After removing the PDMS mold, the replicated NOA61 grating can be coated with metal layers by thermal evaporation.

3. Grating-coupled Surface Plasmon Resonance in the conical mounting: simulation and results
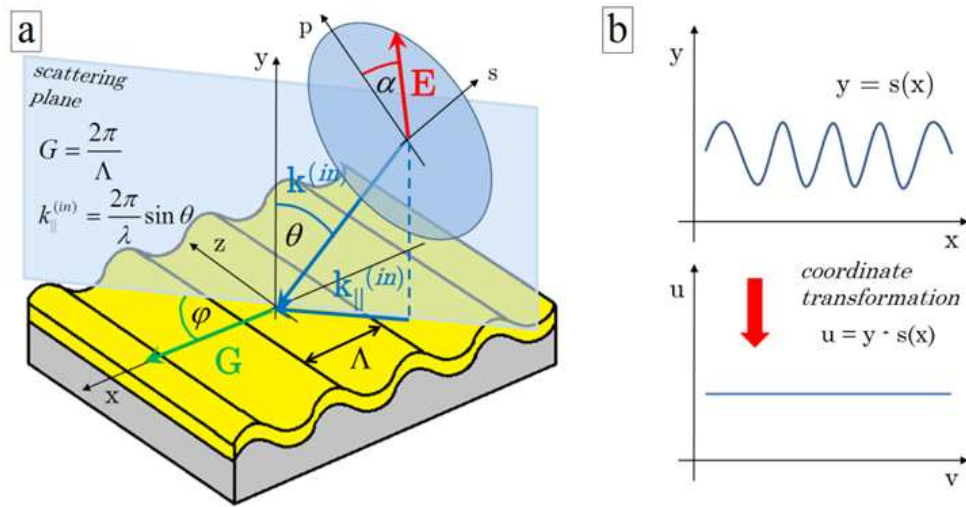
3.1. Chandezon's method

A rigorous approach is necessary in order to exactly solve the problem of a monochromatic plane wave incident on a patterned surface and to simulate the optical response of such multilayered patterned structures. In the past decades, several numerical methods have been developed in order to compute the optical response of periodically modulated multilayered stacks. Among these algorithms, Chandezon's method (hereafter the C-method) revealed itself as one of the most efficient techniques for a rigorous solution of smooth grating diffraction problem. The algorithm is a curvilinear coordinate modal method by Fourier expansion that has gone through many stages of extension and improvement. The original theory was formulated by J. Chandezon et al. [23][24], for uncoated perfectly conducting gratings in classical mountings. Various author extended the method to conical diffraction gratings [25]. G. Granet et al. [26], T.W. Preist et al. [27] and L. Li et al. [28] allowed the various profile of a stack of gratings to be different from each other, although keeping the same periodicity. Solving the vertical faces case in a simple manner, J.P. Plumey et al. [29] have showed that the method can be applied to overhanging gratings.

In the numerical context, L. Li improved the numerical stability and efficiency of the C-method [30][31].

3.2. The coordinate transformation

The setup is as it follows: the grating profile is described by a differential curve $y = s(x)$, periodic in the x-direction with periodicity Λ. The basic feature of the C-method consists in the choice of a non-orthogonal coordinate system that maps the interfaces between different media to parallel planes:

$$u = y - s(x)$$
$$v = x \qquad (2)$$
$$w = z$$

Figure 5. a) Scheme of the reference frame x-y-z and incidence angles θ (polar angle), φ (azimuth) and α (polarization). b) Pictorial description of the coordinate change effect under Chandezon's method.

Since it is a global coordinates transformation, Maxwell's equations covariant formalism is necessary. In a source-free medium the time-harmonic Maxwell equations in term of the covariant field component can be written as [32]

$$\partial_i \sqrt{g} g^{ij} E_j = 0 \qquad (3)$$

$$\frac{1}{\sqrt{g}} \varepsilon^{ijk} \partial_j E_k = i\mu \frac{\omega}{c} g^{ij} H_j \qquad (4)$$

$$\partial_i \sqrt{g} g^{ij} H_j = 0 \qquad (5)$$

$$\frac{1}{\sqrt{g}} \varepsilon^{ijk} \partial_j H_k = -i\varepsilon \frac{\omega}{c} g^{ij} E_j \qquad (6)$$

ε^{ijk} being the completely antisymmetric Levi-Civita tensor[1]. The parameter g is the determinant of the contravariant metric tensor g^{ij}, ε and μ are respectively the dielectric permittivity and the magnetic permeability of the medium. The covariant form[2] g_{ij} is the following:

$$g = \begin{pmatrix} 1+s'^2 & s' & 0 \\ s' & 1 & 0 \\ 0 & 0 & 1 \end{pmatrix} \tag{7}$$

In this case $g = 1$, since the coordinate transformation conserves the volume.

The reference frame is the following: the y-axis is perpendicular to the grating plane and the grating vector $\mathbf{G}$ is oriented along the x-axis positive direction. The scattering plane is perpendicular to the grating plane and forms an azimuth angle φ with the grating symmetry plane (see Figure 5.a). This reference frame has been chosen in order to simplify the coordinate transformation and the form of the metric tensor after an azimuthal rotation: under this convention, the grating is kept fixed and the scattering plane azimuthally rotates.

The incident wavevector $\mathbf{k}^{(in)}$ is given by:

$$\mathrm{k}^{(i)} = \frac{\omega}{c}\left(\sin\theta\cos\varphi, -\cos\theta, \sin\theta\sin\varphi\right) = (\alpha_0, -\beta_0, \gamma) \tag{8}$$

and the wavevector of the n-th diffraction order has the following form:

$$\mathrm{k}^{(n)} = \left(\alpha_n, \beta_n, \gamma\right) \tag{9}$$

where

$$\begin{aligned} \alpha_n &= \alpha_0 + n \cdot G \\ \beta_n &= \sqrt{k^{(i)2} - \alpha_n^2 - \gamma^2} \end{aligned} \tag{10}$$

With these definitions and after some algebraic manipulations, curl equations can be rearranged into the following system of differential equations in the tangential components (H_x, H_z, E_x, E_z) unknown:

$$\frac{\partial H_x}{\partial u} = i\omega\varepsilon E_z + \frac{\partial}{\partial x}\left(\frac{s'}{1+s'^2}H_x\right) + \frac{\partial}{\partial x}\left(\frac{1}{1+s'^2}\frac{i}{\omega\mu}\frac{\partial E_z}{\partial x} + \frac{1}{1+s'^2}\frac{\gamma}{\omega\mu}E_x\right) \tag{11}$$

---

[1] ε^{ijk} equals 1 if (i,j,k) is an *even* permutation of $(1,2,3)$, -1 if it is an *odd* permutation, 0 if any index is repeated.

[2] $g_{i'j} = \Lambda^i{}_{i'}\Lambda^i{}_{j'}\delta_{ij}$ where δ_{ij} is Kronecker's delta, $\Lambda^i{}_j$ is the Jacobi's matrix associated to the coordinate transformation: $\Lambda^i{}_j = \partial x^i/\partial x^j$. The metric tensor g_{ij} allows calculating the covariant components v_i of a vector v from the contravariant ones v^j and vice-versa: $v_i = g_{ij}v^j$, $v^i = g^{ij}v_j$.

$$\frac{\partial E_z}{\partial u} = \frac{s'}{1+s'^2}\frac{\partial E_z}{\partial x} + \frac{1}{1+s'^2}\frac{\gamma}{\omega\varepsilon}\frac{\partial H_z}{\partial x} + \frac{1}{1+s'^2}\left(i\omega\mu - i\frac{\gamma^2}{\omega\varepsilon}\right)H_x \tag{12}$$

$$\frac{\partial H_z}{\partial u} = \frac{s'}{1+s'^2}\frac{\partial H_z}{\partial x} - \frac{1}{1+s'^2}\frac{\gamma}{\omega\mu}\frac{\partial E_z}{\partial x} - \frac{1}{1+s'^2}\left(i\omega\varepsilon - i\frac{\gamma^2}{\omega\mu}\right)E_x \tag{13}$$

$$\frac{\partial E_x}{\partial u} = -i\omega\mu H_z + \frac{\partial}{\partial x}\left(\frac{s'}{1+s'^2}E_x\right) - \frac{\partial}{\partial x}\left(\frac{1}{1+s'^2}\frac{i}{\omega\varepsilon}\frac{\partial H_z}{\partial x} + \frac{1}{1+s'^2}\frac{\gamma}{\omega\varepsilon}H_x\right) \tag{14}$$

where we used the following relation:

$$\frac{\partial F_i}{\partial z} = i\gamma F_i \tag{15}$$

where F_i may stand for (H_x, H_z, E_x, E_z). In fact, since the grating vector has no components in the z-direction, the z-component γ of the incident momentum is conserved and is a constant parameter of the problem.

3.3. Numerical solution and boundary conditions

As suggested by Bloch-Floquet's theorem [33], thanks to the periodicity of the media in the x-direction, a generic field can be expanded in pseudo-Fourier series:

$$F(x,u,z) = e^{i\gamma z}\sum_{m=-\infty}^{+\infty}F_m(u)e^{i\alpha_m x} \tag{16}$$

where $F_m(u)$ is a function periodic in x. Likewise, also the profile functions $C(x)$ and $D(x)$ are periodic in x and can be expanded as well. Laurent's rule can been applied for the Fourier factorization, assuming the continuity of profile function derivative [34]. In the case of sharp edges instead, equations should be rearranged in order to make the inverse-rule factorization applicable [35]. Since in our case of interest the grating profile is a regular function, we can apply Laurent's factorization. After truncation to a finite order N [36] , the problem consists in the numerical solution of a system of $8N+4$ first order differential equations in each medium:

$$-i\frac{\partial U}{\partial u} = TU \tag{17}$$

The problem is led to the diagonalization problem of the matrix T and the solution U^j in the j-th medium can be expressed as a function of eigenvectors V_q^j and eigenvalues λ_q^j of the matrix T:

$$U^j(u) = \sum_q b_q^j V_q^j e^{i\lambda_q^j u} \tag{18}$$

where b_j^q are the weights of the corresponding eigenmodes in the expansion. Thereafter boundary conditions in each medium must be imposed: continuity of the tangential components at each interfaces and outgoing-wave conditions in the first (air) and last (substrate) media [24]. This leads to a system of $8N+4$ equations in $8N+4$ unknowns that is now possible to be solved numerically. Once the mathematical problem has been solved, the electromagnetic fields can be computed inside each j-th medium:

$$F^j\left(x,u,z\right)=e^{i\gamma z}\sum_{m=-N}^{+N}\sum_{n=-N}^{+N}F_{mn}^j e^{i\lambda_n^j u}e^{i\alpha_m x}\tag{19}$$

where F^j stands for (H_x, H_z, E_x, E_z), and F^j_{mn} are the j-field mn-Fourier weight. Transversal components (H_y, E_y) are calculated from Maxwell's equations as a function of the tangential components. By applying the metric tensor to covariant components F_j, the contravariant components F^j, which represent the physical fields, can be obtained. For incident wavelength λ, polar and azimuth angles (θ, φ) and polarization α, the implemented algorithm yields the spatial dependency of the diffracted fields everywhere in space for the modelled grating stack. An estimation of reflection and transmission coefficients for the different diffraction orders, in particular transmittance and reflectivity values (0-diffraction orders) can be obtained. By analysing both real and imaginary parts of eigenvalues λ_q^j, it is possible to distinguish between propagating and evanescent modes, which respectively contribute to the far-field and the near-field parts of the solutions. Thus by selecting only the evanescent contributions in the configurations where SPPs are excited, it is possible to describe the localized plasmonic fields of the excited modes.

3.4. Numerical results and comparison with experimental data

3.4.1. Grating optimization

C-Method has been implemented in MATLAB® code in order to compute the optical response of sinusoidal metallic gratings and simulations have been performed [37] with truncation order $N = 6$. The stack reproduces the typical multilayer bi-metallic gratings fabricated in laboratory by laser interference lithography in the so called Lloyd's configuration (section 2.1). Simulation code provides a fundamental tool in order to select the grating geometries that exhibit the best optical features and provide to nanofabrication the optimal windows of process for the realization of optimized optical components. Silver thickness must be properly chosen in order to optimize the plasmonic response of the structure and the optimal thickness strictly depends on the amplitude of grating modulation. Simulations have been performed at the incident wavelength $\lambda = 632$ nm for several values of the profile amplitude in the range 20-60 nm and for varying silver thickness in the range 10-80 nm, in the case of a sinusoidal grating with fixed period $\Lambda = 500$ nm, gold thickness 7 nm and a fixed chromium adhesion layer of 5 nm over a NOA61 substrate.

As Figure 6.a shows, for each amplitude value a silver thickness exists that optimizes the coupling of incident light with SPP modes, i.e. that minimizes the depth of the reflectivity

dip. Figure 6.b shows some examples of reflectivity curves in angular scan for optimal combinations of profile amplitude and silver thickness. For increasing amplitude of the grating profile, the optimal silver thickness decreases (Figure 6.a) and the corresponding reflectivity curve becomes broader (Figure 6.b). This result seems to suggest the choice of a shallow grating modulation with the evaporation of the corresponding optimal thickness of silver: for an amplitude A = 30 nm the optimal silver thickness is around 80 nm. On the other hand, the coating with a great quantity of metal could affect the preservation of the original pattern and cause lack in accuracy of the final profile. The evaporation of about 40 nm of silver instead, could assure the control of the grating profile and at the same time a reasonable value for the reflectivity-dip FWHM (Full Width at Half Maximum).
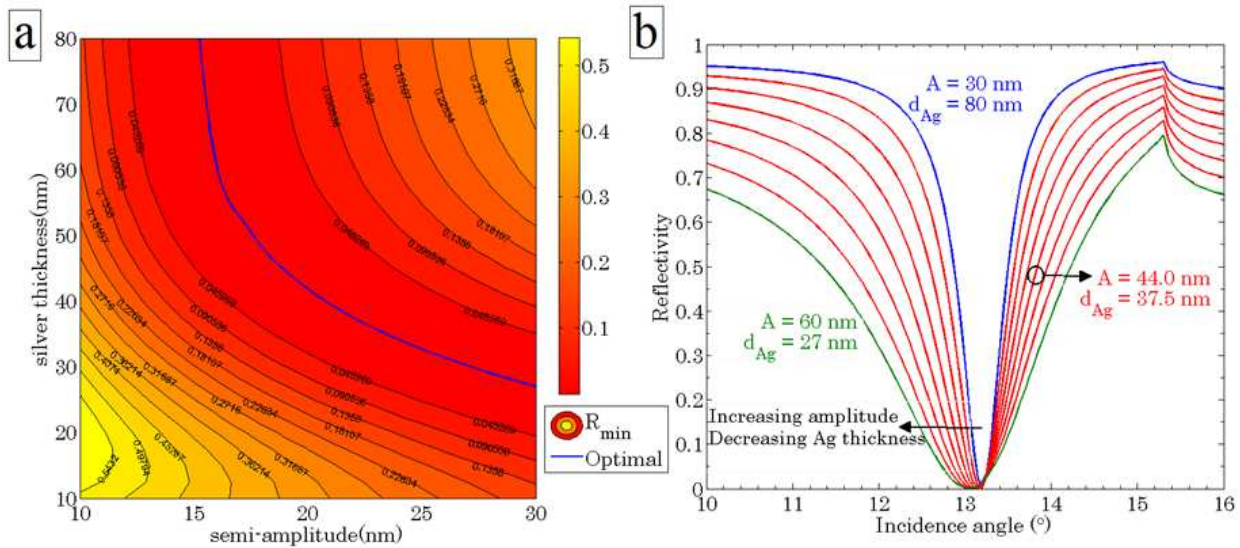

Figure 6. a) Reflectivity minimum as a function of profile semi-amplitude and silver-film thickness for fixed period 500 nm, fixed gold-film thickness 7 nm, incident wavelength 632 nm (sinusoidal profile). Superimposed blue line: optimal configurations. b) Simulated reflectivity in angle scan for values of amplitude and silver thickness along the optimal configuration line in (a): amplitude range 30-60 nm, step 4 nm.

3.4.2. Comparison with experimental data

Numerical results have been compared with experimental data from reflectivity analysis of the corresponding fabricated sample. The simulated stack reproduces the multilayer structure of the considered grating: air (upper medium), Au (8 nm), Ag (35 nm), Cr (9 nm), photoresist (70 nm), Si (substrate). For each layer the optical constants (refractive index n, extinction coefficient k) have been extrapolated from ellipsometric analysis and have been inserted into the code. From AFM analysis, the grating profile results sinusoidal with period 505 nm and peak-to-valley amplitude 26 nm.

As figure 7 shows, numerical estimation of grating reflectivity well fits experimental data within instrumental errors (~2%). Reflectivity measurements have been performed by means of the monochromatized 75 W Xe-Ne lamp of a spectroscopic ellipsometer VASE (J. A. Woollam), with angular and spectroscopic resolution respectively 0.001° and 0.3 nm
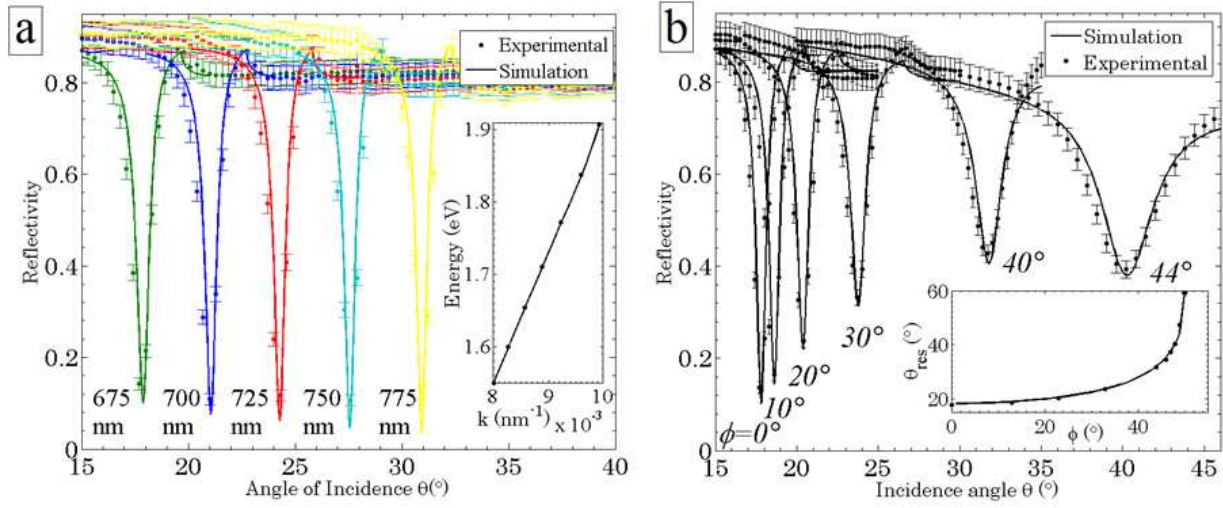
Figure 7. a) Reflectivity spectra for angular interrogation at null azimuth $\varphi = 0°$ for incident wavelengths λ in the range 675-775 nm with step 25 nm, p-polarization ($\alpha = 0°$). Experimental data points and simulation results (solid lines). In the inset graph: SPP dispersion curve $\omega - k$. b) Reflectivity spectra for angular interrogation, variable azimuth φ for the $\lambda = 675$ nm, p-polarization. In the inset graph: resonance angle θ_{res} as a function of the azimuth angle φ: experimental points and simulation curve (solid line).

Figure 7.a shows reflectivity spectra for angular interrogation at null azimuth $\varphi = 0°$ for incident wavelengths λ in the range 675-775 nm with step size 25 nm, p-polarization ($\alpha = 0°$). In angular interrogation, the reflectivity dip shifts towards greater resonance angles for increasing wavelength. Numerical results perfectly reproduce experimental data trends and from dip position it is possible to reconstruct SPP dispersion (Figure 7.a, inset graph).

Figure 7.b exhibits reflectivity spectra in angular interrogation for the azimuth values $\varphi = 0°$, 10°, 20°, 30°, 40°, 44°, incident wavelength $\lambda = 675$ nm and p-polarization ($\alpha = 0°$).

4. Sensitivity enhancement by azimuthal control

The analysis of the wavevector components allows a description of double SPP excitation using the schematic shown in Figure 8. The excitation of SPPs on a grating is achieved when the on-plane component $k_{||}^{(in)}$ of the incident light wavevector and the diffracted SPP wavevector k_{SPP} satisfy the momentum conservation condition:

$$
\begin{aligned}
\mathrm{k}_{SPP} &= \mathrm{k}_{||}^{(in)} + n \cdot \mathrm{G} \\
\mathrm{k}_{SPP} &= \frac{2\pi}{\lambda} \sin\theta_{res} \cdot (1,0) - \frac{2\pi}{\Lambda}(\cos\varphi, \sin\varphi)
\end{aligned}
\tag{20}
$$

where θ_{res} is the resonance polar angle, φ is the azimuth angle, Λ is the grating pitch, λ is the illuminating wavelength. Only the first diffraction order ($n = -1$) is considered because in our cases of interest, grating momentum G is always greater than k_{SPP}.

All quadrants of the circle in Figure 8 can be explored for SPP excitation as long as momentum conservation is satisfied. For symmetry reason, only k_y positive half space is

considered. Soving eq. (20) in the resonance angle unknown, the following expression is obtained as a function of the azimuth angle φ.

$$\theta_{\mp} = \arcsin\left(\frac{\lambda}{\Lambda}\cos\varphi \mp \sqrt{M(\lambda)^2 - \left(\frac{\lambda}{\Lambda}\sin\varphi\right)^2}\right) \tag{21}$$

where $M(\lambda) = k_{SPP}/(2\pi/\lambda)$.

The largest circle in the k-space represents equi-magnitude G vectors at different azimuthal orientation. The two smaller circles represent all possible k_{SPP} vectors with equal magnitude respectively before and after surface functionalization and whose modulus, for shallow gratings, can be approximated by [2]:

$$k_{SPP} = \frac{2\pi}{\lambda}M(\lambda) = \frac{2\pi}{\lambda}\sqrt{\frac{\varepsilon_m\varepsilon_{eff}}{\varepsilon_m + \varepsilon_{eff}}} \tag{22}$$

where ε_m and ε_{eff} are the dielectric permittivity of the metal and the dielectric side respectively. After functionalization, SPP modulus increases because of the small increase in ε_{eff} due to the surface coating.
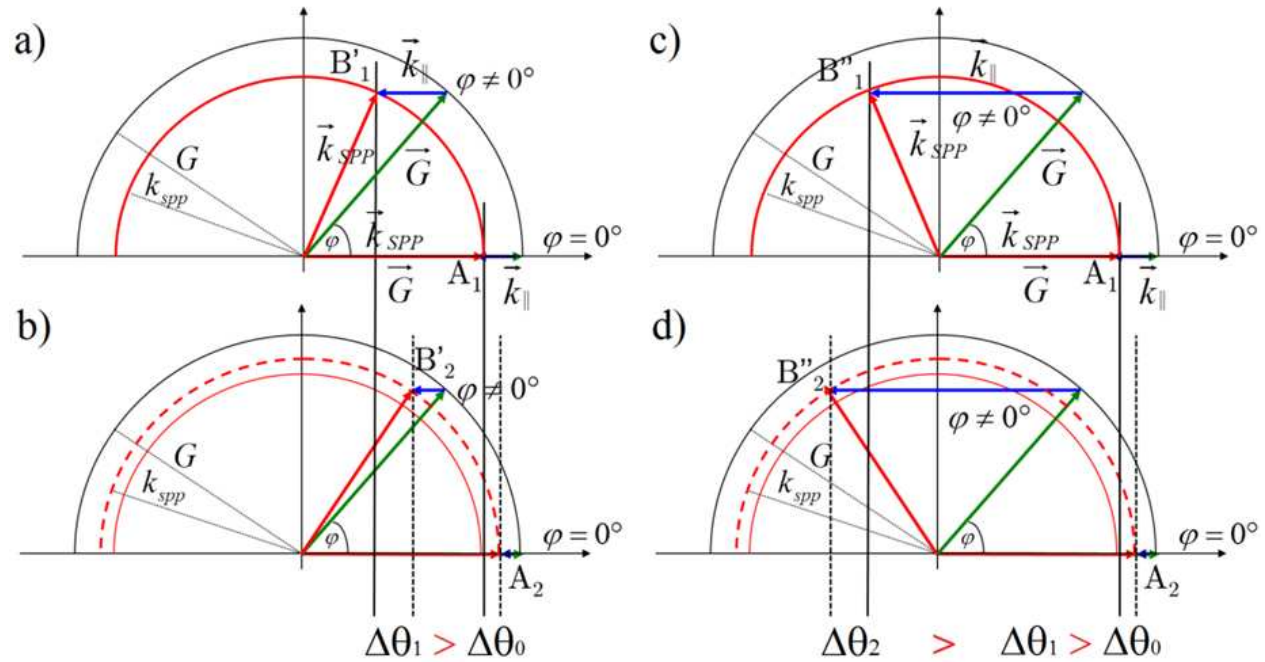
Figure 8. Schematic picture of wave-vector combination at SPP resonance ($n = -1$). The large circle represents equi-magnitude G vectors. The smaller circles represent equi-magnitude k_{SPP} vectors before (a, c), and after (b, d) surface functionalization for the first (a, b) and the second (c, d) SPP excitation. The blue arrows represent the photon on-plane wavevector and the red arrows represent the SPP propagation direction. The letters A and B represent the vector with azimuthal rotation $\varphi = 0°$ and $\varphi \neq 0°$ respectively.

The dashed line at the tip of the circle of radius G represents the x-component of the photon wave-vector $k_{||}^{(in)}$, the only component that participates in SPP excitation. The line is scaled linearly in $\sin\theta$ so that the full length of the line at the incident angle θ of 90° corresponds to the maximum value of $k_{||}^{(in)}$. The intersections of the $k_{||}^{(in)}$ dashed horizontal line with the smaller k_{SPP} circle determine the conditions for which eq. (20) is satisfied and allows the identification of both incident angle θ_{res} for SPP resonance excitation and SPP propagation direction β. We consider first the case of the uncoated sample - the smallest of the semicircles. For example, point B on the G circle is identified by the azimuthal angle φ and allows the excitation of SPP at two possible conditions: B_1' and B_1'', with β^- and β^+ respectively. Within the double SPP range (point B), a small increment in wavelength makes the points B_1' and B_1'' merge to form a very broad. On the contrary, at $\varphi = 0°$ (point A_1) it is clear that the photon wave-vector can intersect the SPP circle only in the first quadrant but not the second, thus exciting only a single SPP for each wavelength. The same argument is applicable for light exciting SPP on the functionalized sample. Due to the larger k_{SPP}, a different excitation condition is expected. The intersection points changes from B_1' and B_1'' to B_2' and B_2'' and from A_1 to A_2. The sensitivity of the GCSPP is higher at high azimuthal angles because the condition for double SPP excitation around the circumference of the k_{SPP} circle generates a shifts in k-space between points B_1' and B_2', which is much larger than that between points A_1 and A_2 provided by a single SPP excitation condition for $\varphi = 0°$. The estimated refractive index sensitivity S of this configuration can be defined as:

$$S = \frac{\partial\theta}{\partial n} = \frac{\partial\theta}{\partial k_{||}^{(in)}} \frac{\partial k_{||}^{(in)}}{\partial k_{SPP}} \frac{\partial k_{SPP}}{\partial n} \tag{23}$$

In order to calculate S, we assumed the rippling amplitude A of the grating is so shallow ($A/\Lambda \sim 0.05$ in our case of interest) that the dispersion curve of SPPs traveling at the metal-dielectric interface of a grating can be approximated by the case of a flat sample (eq. (22)). The analytical expression for the sensitivity in angular interrogation can be found as:

$$S = -\frac{1}{\cos\theta_{res}} \left(\frac{M}{n_0}\right)^3 \frac{\sqrt{\dfrac{1}{\Lambda^2} + \dfrac{\sin^2\theta_{res}}{\lambda^2} - \dfrac{2\cos\varphi\sin\theta_{res}}{\Lambda\lambda}}}{\dfrac{\cos\varphi}{\Lambda} - \dfrac{\sin\theta_{res}}{\lambda}} \tag{24}$$

where M is defined in eq. (22), n_0 is the refractive index of the surrounding dielectric medium, the resonance angle θ_{res} is given by eq. (21) for fixed λ.

The functional behavior of sensitivity for the first and second SPP dip is shown in Figure 9 for a typical wavelength of $\lambda = 606$ nm. Both sensitivities diverge when φ approaches its critical value φ_{MAX}, i.e. the maximum φ angle that supports SPP resonances. In this configuration, incident photon momentum is tangential to the k_{SPP} circle and its length equals the x-component of the grating momentum so that the denominator in eq. (24) becomes null. Another condition for second dip sensitivity singularity is when φ approaches the critical azimuthal angle, φ_c, necessary to excite double SPP resonances, namely when the

full length of the incident photon momentum is required to intersect the edge of the k_{SPP} circle. Since the incident angle $\theta = 90°$, $\cos\theta_{res}$ in the denominator of the first term eq. (24) approaches 0 and S diverges.
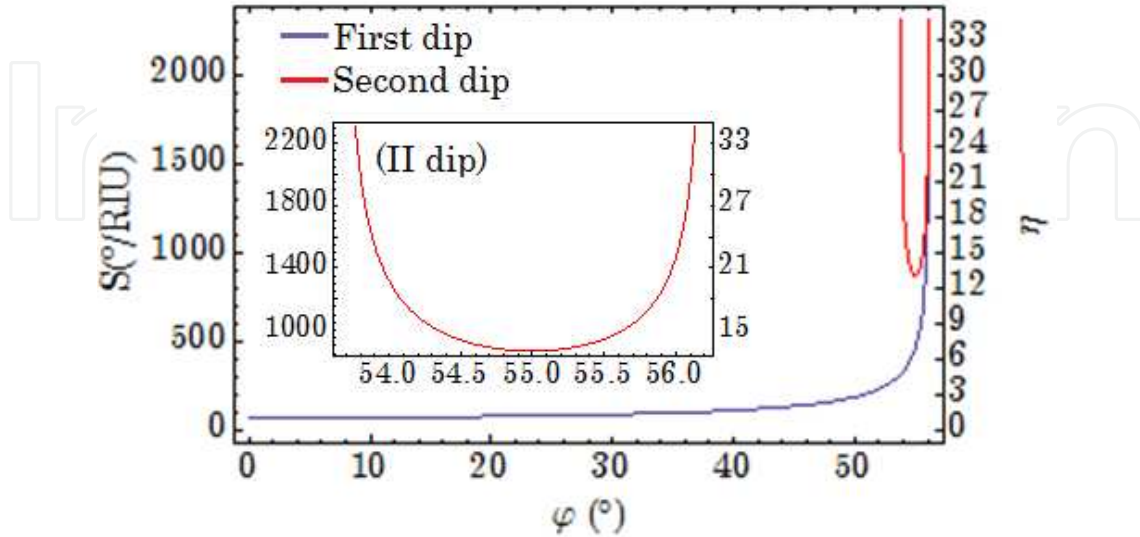

Figure 9. Sensitivity S_θ as a function of grating azimuthal angle φ for the two dips in SPR sensor with angular interrogation. The right y-scale refers to sensitivity values normalized to the first dip sensitivity at $\varphi = 0°$: $\eta = S_\theta(\varphi)/ S_\theta(\varphi=0°)$.

Although azimuth φ values close to the critical values provides a great enhancement in S (up to 2400°/RIU, 35 times higher than the case $\varphi = 0°$), these configurations should be avoided because of experimental limits. For $\varphi \cong \varphi_c$, θ_{res} becomes large (>70-80°) and broad, becoming impossible to resolve the SPP minimum. In addition, when $\varphi \cong \varphi_{MAX}$ the two resonance dips merge into a single broad dip which makes the two minima hardly distinguishable. Thus only limited parts of the azimuthal angular range are suitable to enhance sensitivity significantly. The best conditions correspond to the middle of the "U-shape" of second dip functional behavior (Figure 9) where the sensitivity ranges from 900°/RIU to 1100°/RIU, about 15 times higher than $\varphi = 0°$ whose value is 67°/RIU. The sensitivity computed for the first SPP dip is smaller all over this range but it still provides values of the order of 500°/RIU.

4.1. Application to functionalization detection

Sensitivity enhancement with azimuthal rotation has been tested with a C12-functionalization of a bimetallic (37Ag/7Au) grating, period 487 nm, amplitude 25 nm. Reflectivity analyses performed before and after C12-coating are collected in Figure 10.a-b. The figure shows the experimental evidence of the azimuth rotation, where reflectivity spectra are reported at different wavelengths. As a reference Figure 10.a reports the reflectivity spectra using the conventional GCSPR configuration with $\varphi = 0°$. In this configuration, the difference in the reflectivity minima resonance angle θ_{res} before and after

C12 is typically less than 0.05°. On the contrary after an azimuthal rotation of the grating to an angle φ of about 60°, larger angular differences can be observed between the reflectivity dips (Figure 10.b). The resonance shift can reach values up to 3.1° as for the incident wavelength $\lambda = 618$ nm. By increasing wavelength from 606 to 618 nm, the two resonance dips in the reflectivity spectra get closer while resonance shift increases from 1.8° to 3.1°, until the two resonances merge together into a single broad dip at 620 nm.
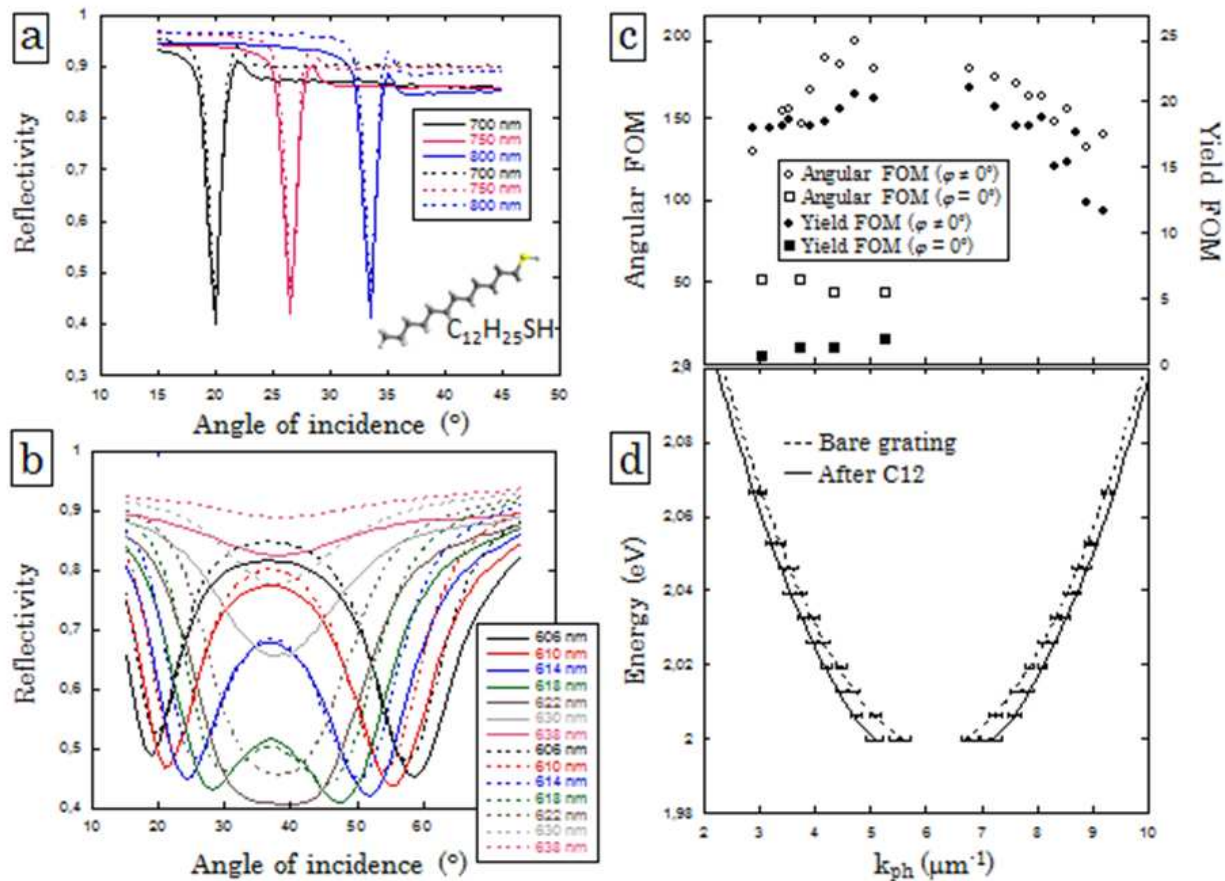
Figure 10. Comparison of SPR spectrum between uncoated (dashed line) and C12-coated (solid line) Au grating. (a) Grating with $\varphi = 0°$, for incident wavelength $\lambda = 700\text{-}800$ nm, step 50 nm, and (b) $\varphi = 60°$, (2 SPPs by single wavelength excitation condition), for incident wavelength $\lambda = 606\text{-}638$ nm, step 4 nm. c) Figure of merit for yield ($\cdot$, $\blacksquare$) and angular (o, $\square$) interrogation of the SPR reflectivity minima. (d) Energy dispersion curve for the $k_{\parallel}^{(in)}$ necessary for SPP excitation before (dashed line) and after (solid line) C12 SAM functionalization.

The experimental determinations of the wavevector $k_{\parallel}^{(in)}$ of the incoming light necessary for the SPP excitation have been successfully fitted with the help of eq. (20), using as fitting parameters only the effective index of refraction and azimuthal angle (see Figure 10.d). After surface functionalization we have determined a total increment in index of refraction equal to $\Delta n = 0.00357 \pm 0.00007$ RIU. This is a value that agrees with the

estimation of RIU performed for effective refractive index change generated by a full surface coverage of close-packed self assembled C12 molecules, considering their length 1.46 nm with dielectric constant ε_{C12} = 2.12. Also the theoretical sensitivity determination (Figure 9) is in good agreement with the experimental determination obtained as a ratio between Δn, the angular differences before and after C12 coating and the Δn determination. The average experimental sensitivity is of the order of 520°/RIU for the first dip and reaches maximum values of 857°/RIU for the second dip. The final error of the refractive index determination has been estimated on the basis of chi-square minimization based on *a priori* determination of the SPP angular position. The reflectivity minima of this preliminary data set have been determined with a typical uncertainty of 0.07°. However the *a posteriori* determination of the SPP angular average deviation with respect to the dispersion curve best fit is much smaller, on the order of 0.015°, as can be confirmed by a simple graphical inspection. Taking into account this more realistic value for the final evaluation of the uncertainty, the value of 10^{-5} RIU. However, because our experimental system has an instrumental resolution of 0.001°, we believe it will be possible to greatly decrease the present angular uncertainty by increasing the statistical signal-to-noise ratio and using appropriate algorithms for data analysis. We expect that experimental uncertainties of Δn on the order of $5 \cdot 10^{-7}$ RIU is achievable. In order to better describe the detection improvement given by azimuthal rotation, we have also measured the typical figure of merit for angular and yield interrogation respectively defined as:

$$FOM_\theta = \frac{S_\theta}{\Delta\theta_{FWHM}}$$

$$FOM_Y = \frac{Y_{coat} - Y_{uncoat}}{Y_{uncoat}}$$

(25)

where $\Delta\theta_{FWHM}$ is the angular full width at half maximum of the reflectivity minima, whereas Y_{coat} and Y_{uncoat} are the minimum yield of the reflectivity spectra collected before and after C12 functionalization at SPR resonances.

Figure 10.c shows the angular and yield *FOM* at zero and after the azimuthal rotation for all the reflectivity spectra. It clearly appears an enhancement of both the figures of merit after the azimuthal rotation that amounts up to a factor 4 and 10 for the angular and yield *FOM* respectively. This means that the distance between two dips, before and after the functionalization, scales with a factor greater than the enlargement of the reflectivity dip width. Moreover, it is worth to note that the reflectivity yield is even more sensitive than the angular position. It clearly appears from the reflectivity spectra of Figure 10.b that whereas the minimum yield between coated and uncoated are almost the same for zero azimuth, it changes dramatically after azimuthal rotation. Finally, we note that both the angular and the yield *FOM* have similar functional behavior: they increase approaching the condition of two dips merging when $\beta_+ = \beta_- = 90°$.

4.2. Application to solution analysis

A microfluidic cell was fabricated in PDMS by soft-lithography technique and embodied to the metallic grating. The considered metallic gratings exhibits a sensitivity $S_\theta(0°) =$ 64.9°/RIU for $\lambda = 840$ nm (Figure 11.a-b). As demonstrated in the previous section, angular sensitivity S_θ can be improved just with an azimuthal rotation of the grating plane. For a same fixed concentration of 10g(Nacl) in 200ml(water), corresponding to a refractive index variation with respect to distilled water $\Delta n = 9.6 \cdot 10^{-3}$ [38], reflectivity spectra have been collected for increasing azimuth angle φ up to 43° at the same incident wavelength. As Figure 11.c shows, resonance angle shift increases monotonically in modulus with increasing azimuth angle from $\Delta\theta(0°) = 0.59°$ to $\Delta\theta(43°) = 5.57°$ corresponding to a sensitivity enhancement $\Delta\theta(43°)/\Delta\theta(0°) = 9.5$ of almost one order of magnitude: $S_\theta(43°) =$ 616.8°/RIU.
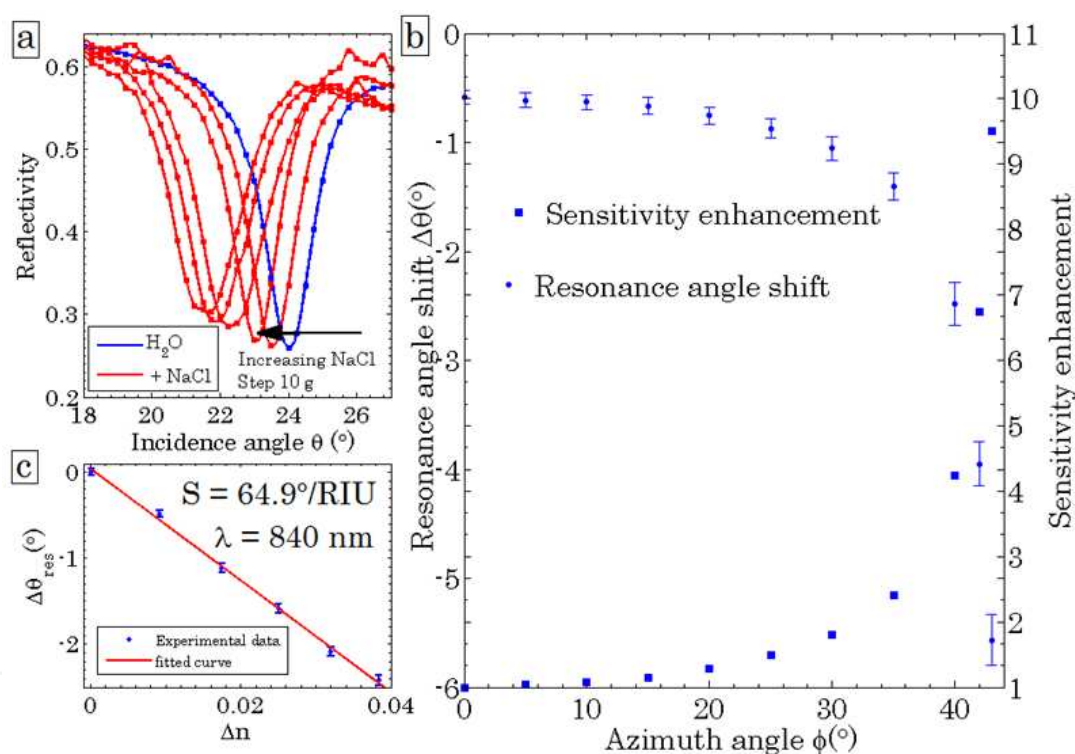
Figure 11. (a) Reflectivity in polar angular scan at incident wavelength 840 nm, null-azimuth, *p*-polarization, for increasing NaCl concentration in water solution: 0-50 g, step 10 g, in 200 ml of water. (b) Resonance angle shift as a function of refractive index variation of water solution with increasing NaCl concentration. (c) Resonance angle shift and sensitivity enhancement as a function of azimuth angle in the range 0-43°. NaCl concentration: 10g in 200ml of water ($\Delta n = 9.6 \cdot 10^{-3}$).

This sensitivity-enhancement technique with azimuthal rotation has been exploited to reveal a lower sodium-chloride concentration than the previous one. A mass of 0.56 g has been dissolved into 200 ml of water and the resulting refractive index change is $\Delta n = 5.4 \cdot 10^{-4}$. With this solution flowing through the microfluidic cell, reflectivity measurements have been performed for increasing grating rotation (Figure 12). The inset picture in Figure 12 shows the reflectivity spectra before and after salt dissolution for null azimuth and after

grating azimuthal rotation up to 43°. While in the classical mounting, i.e. null azimuth, this variation is not detectable within the experimental error, in conical mounting instead grating azimuthal rotation increases SPR sensitivity and thus the system allows revealing the resonance angle shift. Resonance dips become broader when azimuthal angle increases, however the resonance angle shift $\Delta\theta$ scales with a factor greater than the enlargement of the dip full width half maximum $\Delta\theta_{FWHM}$. Thus the angular figure of merit FOM_θ increases and the detection improvement by azimuthal rotation is preserved. In this case we have $FOM_\theta(43°)/FOM_\theta(0°)\cong4.3$.
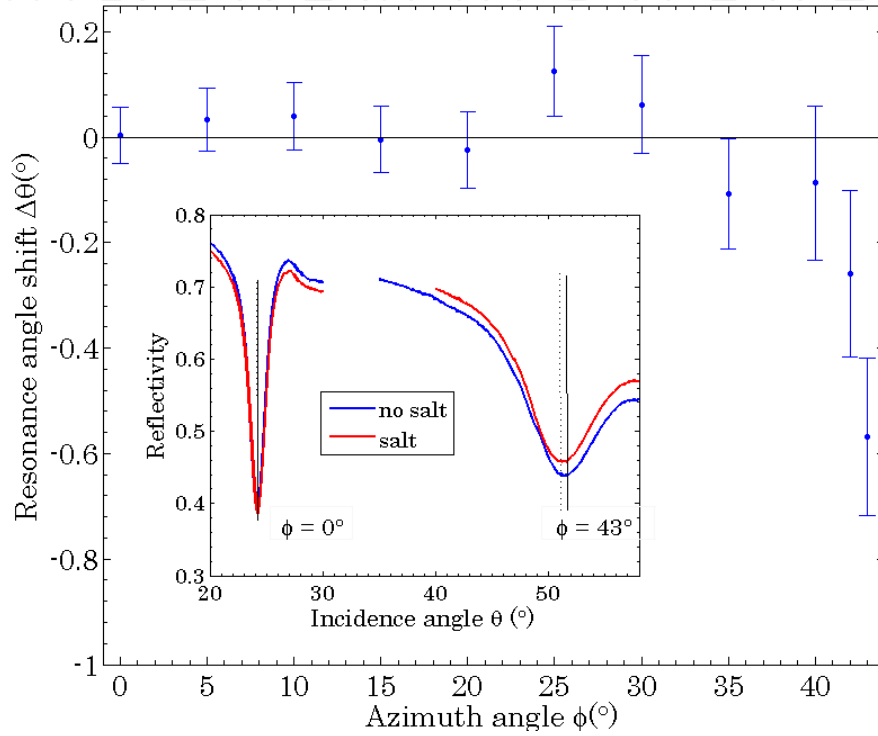
Figure 12. Resonance angle shift as a function of azimuth angle for sodium-chloride concentration: 0.56g/200 ml(water), $\Delta n = 5.4 \cdot 10^{-4}$. In the inset graph: reflectivity curve before (blue) and after (red) NaCl dissolution into water, angular scan for azimuth values $\varphi = 0°$ and 43°.

5. Innovative SPR with polarization modulation

In previous sections we experimentally and theoretically described the effects of grating azimuthal rotation on surface plasmon excitation and propagation. More SPPs can be supported with the same illuminating wavelength and a sensitivity enhancement of al least one order of magnitude is achievable than that in the conventional configurations. Here we consider how the symmetry breaking with grating rotation makes polarization have a fundamental role on surface plasmon polaritons excitation. As Figure 7.b shows, p-polarization becomes less and less effective for increasing azimuthal rotation and the reflectivity depth decreases. If the polar angle is fixed at resonance and a polarization scan is performed, the minimum of reflectivity R_{min} exhibits a harmonic dependency on the incidence polarization α with a periodicity of 180° (Figure 13):

$$R_{\min} = f_0 - f_1 \cos(2\alpha + \alpha_0)$$ (26)

where f_0, f_1 and α_0 are fitting parameters that depend on the incidence angles θ and φ, incident wavelength λ and on the optical properties of the stack (thickness and dielectric permittivity of each layer). While for null azimuth $\alpha_0 = 0°$ and p-polarization is the most effective for SPP excitation, after grating rotation the phase term α_0 is non null and strictly depends on the incidence angles. By assuming that only the electric field component lying on the grating symmetry plane is effective for SPP excitation, on the basis of a vectorial approach, an analytical expression can be obtained [18] for the optimal polarization α_{opt} as a function of the azimuth angle φ and the resonance angle θ_{res}:

$$\tan\alpha_{\min} = \tan\varphi \cdot \cos\theta_{res}$$ (27)
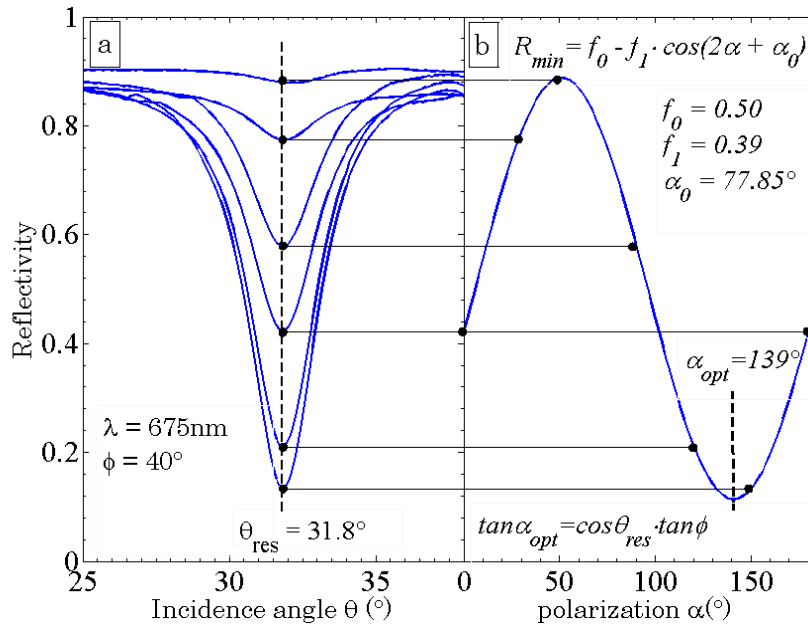
Figure 13. (a) Reflectivity for polar angle scan in the range 25°-38°, step 0.1°, at $\lambda = 675$ nm and azimuth $\varphi = 40°$ for varying incident polarization α in the range 0°-180°, step 30°. (b) Reflectivity minima as a function of polarization and fit curve.

If the grating surface is functionalized, the effective refractive index n_{eff} of the dielectric medium changes and resonance conditions are different. As a consequence of the shift in the resonance angle θ for a fixed azimuth φ, there is a shift $\Delta\alpha_0$ in the phase term α_0:

$$\Delta\alpha_0 = \frac{\partial\alpha_0}{\partial n}\Delta n$$ (28)

This result opens the route to a new GCSPR-configuration with polarization interrogation[39]. In this setup the grating is rotated of an azimuthal angle which is kept fixed. The illuminating wavelength is fixed and the incoming light impinges on the grating at the polar resonance angle. A rotating polarizer between source and sample-holder allows changing the polarization incident on the grating. Reflectivity data collected during a

polarization scan can be fitted using eq. (26) and a variation of fitting parameters, e.g. amplitude f_1 or phase α_0, can be used in order to detect grating functionalization or for solution-concentration analysis, once the system has been properly calibrated.

A metallic grating with a period of 505 nm and amplitude of 26 nm, fabricated by interferential lithography (IL) followed by thermal evaporation of a gold (40 nm) metallic layer over 5 nm of chromium adhesion layer. Optical measurements have been performed in $\theta/2\theta$ symmetric reflectivity configuration, using the 75W Xe lamp of VASE Ellipsometer (J. A. Woollam). A self-assembled monolayer of dodecanethiol was deposited on the gold coated grating surfaces at room temperature [40].

First of all, reflectivity spectra have been collected in angular scan to identify the resonance angle position with a weighted centroid algorithm [41]. In order to exploit the shift enhancement, grating was azimuthally rotated and kept fixed at the value $\varphi = 57.8°$ wherein double SPP excitation is supported for the selected wavelength $\lambda = 625$ nm. In correspondence of the resonance angles, respectively $\theta_- = 30.8°$ and $\theta_+ = 55.1°$ for the first and second dip, a polarization scan has been collected in the range 0-180°, step 10°, before and after C12 functionalization. The same analysis has been performed at the wavelength 635 nm, for the same azimuth, when the two dips merge into a single broad one centered in $\theta = 43°$.
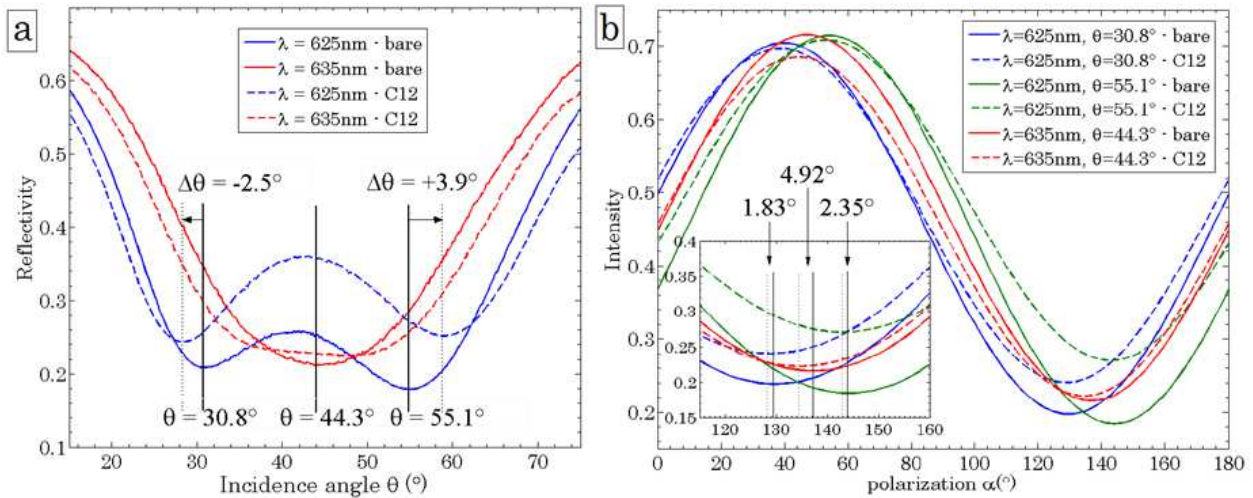
Figure 14. (a) Reflectivity for angular scan in the range 15°-75°, step 0.2°, at $\lambda = 625$ nm (blue lines) and $\lambda = 635$ nm (red lines), azimuth $\varphi = 57.8°$, incident polarization $\alpha = 140°$, before (solid lines) and after (dashed lines) functionalization with C12. (b) Polarization scan for $\lambda = 625$ nm (blue lines: I dip ($\theta_- = 30.8°$), green lines: II dip ($\theta_+ = 55.1°$)), $\lambda = 635$ nm (red lines: merged dips ($\theta = 44.3°$)), azimuth $\varphi = 57.8°$, before (solid lines) and after (dashed lines) C12-coating. Inset picture: phase shifts $\Delta\alpha_0$.

By modelling the effective refractive index change Δn_{eff} with an effective medium approximation [42], it is possible to estimate the corresponding phase sensitivity S_α and moreover to calculate the refractive index resolution:

$$\sigma_{n,\alpha} = \frac{\sigma_\alpha}{S_\alpha} \qquad (29)$$

C12 has been assumed to form a monolayer 1.46 nm-thick with refractive index n=1.458 [43] and results in Δn_{eff} (625 nm) = 50.5 · 10^{-4} and Δn_{eff} (635 nm) = 48.1 · 10^{-4}. In the case of double SPP excitation (λ=625 nm), the phase shifts result $\Delta\alpha_0(I)$=1.834 ± 0.001° (first dip) and $\Delta\alpha_0(II)$= 2.353 ± 0.001° (second dip), corresponding respectively to sensitivity values $S_\alpha(I)$=363.2°/RIU and $S_\alpha(II)$= 465.9°/RIU, refractive index resolutions $\sigma_{n,\alpha}(I)$=2.7 · 10^{-6} RIU and $\sigma_{n,\alpha}(II)$=2.1 · 10^{-6} RIU. For λ=635 nm, we get S_α = 1022.7°/RIU and 2 · 10^{-6} RIU.

Thus refractive index changes of order 10^{-6} RIU are easily detectable and the resolution can be further improved to 10^{-7}-10^{-8} by reducing output noise σ_I or by increasing the number N of the points collected during the polarization scan.

Furthermore this technique provides a resolution at least two order greater than polar angle modulation with the same setup, which results around $\sigma_{n,\theta}$~10^{-4}-10^{-5} RIU. Moreover, while angle-modulation SPR becomes difficult near the merging dip condition, since dip position is hardly detectable, in the polarization-modulation case the analysis is still valid and it assures a greater sensitivity. On the top of that, since the output trend is a well-known function of polarization, this method assures a great accuracy on fitting parameters and their dependence on grating surface conditions provides a solution to detect and quantify surface functionalization or solution concentration. This method assures a competitive resolution down to 10^{-8} and limits the mechanical degrees of freedom just to the polarization control. The option of using an electronic modulator instead of a rotating polarizer, further assures the possibility to realize very compact, fast and low-cost high-resolution plasmonic sensors.

6. Conclusions

Plasmonic gratings have been demonstrated to assure a high-sensitive optical response to surface functionalization and to represent a promising and irreplaceable component for the realization of label-free devices for sensing purposes with considerable performance in refractive index sensitivity and resolution. The problem of designing and realizing metallic gratings for sensing applications has been studied and analysed through each step of the process-chain: simulation - nanofabrication - characterization.

Chandezon's method provides an algorithm for a rigorous and complete analysis of the diffraction problem of a multi-layered patterned. The numerical code provides a precise estimation of grating reflectivity and is an essential tool to design, for given geometry and material choice, the optimal profile that optimizes the coupling strength of incident light with surface plasmon polaritons. Simulation is essential to provide to nanofabrication the proper windows of process for the production of optimized supports.

As regards the nanofabrication of these components, interferential lithography is the preferred method to fabricate periodic pattern with a spatial coherence over large areas,

while grating-replica process by soft-lithography assures the possibility of a fast and cheap throughput of perfectly replicated gratings. With respect to prism-coupling, grating nanofabrication technology assures the possibility to miniaturize and integrate the sensing components without a considerable increase of the total expenditure. Moreover, our results further highlight grating-coupling advantages rather than prism-coupling thanks to the sensitivity enhancement with azimuthal rotation. An enhancement at least one order greater than the conventional mounting has been theoretically and experimentally demonstrated.

If the azimuthal rotation of the grating support increases refractive index sensitivity, on the other hand incident polarization must be tuned in order to best couple incident light and optimize the optical response. The dependence of polarization angle on the resonance conditions suggests the exploitation of a new SPR configuration based on polarization modulation in the conical mounting. The phase term of a polarization scan, which is proportional to the optimal polarization, has been experimentally demonstrated to be a sensitive parameter for surface functionalization analysis. This innovative sensing configuration hugely simplifies the mechanical complexity of the device by limiting the degrees of freedom just to the rotating polarizer and assures the possibility of realizing very compact, fast and low-cost high-resolution plasmonic sensors based on polarization modulation.

Author details

G. Ruffato, G. Zacco and F. Romanato
University of Padova, Department of Physics "G. Galilei", Padova, Italy
Laboratory for Nanofabrication of Nanodevices (LaNN - Venetonanotech), Padova, Italy
Istituto Officina dei Materiali IOM-CNR National Laboratory, Trieste, Italy

Acknowledgement

7. References

[1] Raether H., Surface Plasmons on Smooth and Rough Surfaces and on Gratings. Springer-Verlag, 1988.
[2] Maier S. A., editor. Plasmonics - Fundamentals and Applications. Springer, 2007.
[3] Wood R. W., On a remarkable case of uneven distribution of light in a diffraction grating spectrum, *Philos. Mag*. 4, 396-402 (1902).
[4] Cowan J. J., Arakawa E. T., Dispersion of surface plasmons in dielectric-metal coatings on concave diffraction gratings, *Zeitschrift fur Physik* 235, 97 (1970).

[5] Homola J., Yee S. S., Gauglitz G., Surface plasmon resonance sensors: review, *Sens. Actuators B* 54, 3-15 (1999).

[6] Kretschmann E., *Z. Phys.* 241, 313-324 (1971).

[7] Homola J., Surface Plasmon Resonance Based Sensors. Springer, 2006.

[8] Karlsson R., Stahlberg R., Surface plasmon resonance detection and multispot sensing for direct monitoring of interactions involving low-molecular-weight analytes and for determination of low affinities, *Anal. Biochem.* 228, 274-280 (1995).

[9] Homola J., Koudela I., Yee S. S., Surface plasmon resonance sensor based on diffraction gratings and prism couplers: sensitivity comparison, *Sens. Actuators B* 54, 16-24 (1999).

[10] Hoa X. D., Kirk A. G., and Tabrizian M., Towards integrated and sensitive surface plasmon resonance biosensors: a review of recent progress, *Biosens. Bioelectron.* 23, 151-160 (2007).

[11] Yoon K. H., Shuler M. L., and Kim S. J., Design and optimization of nano-grating surface plasmon resonance sensors, *Opt. Express* 14, 4842-4249 (2006).

[12] Unfricht D. W., Colpitts S. L., Fernandez S. M. and Lynes M. A., Grating-coupled surface plasmon resonance: a cell and protein microarray platform, *Proteomics* 5, 4432-4442 (2005).

[13] Dostalek J., Homola J., Miler M., Rich information format surface plasmon resonance biosensor based on array of diffraction gratings, *Sens. Actuators B* 107, 154-161 (2005).

[14] Alleyne C. J., Kirk A. G., McPhedran R. C., Nicorovici N. A. P., and Maystre D., Enhanced SPR sensitivity using periodic metallic nanostructures, *Opt. Express* 15, 8163-8169 (2007).

[15] Telezhnikova O., Homola J., New approach to spectroscopy of surface plasmons, *Opt. Lett.* 31, 3339-3341 (2006).

[16] Romanato F., Lee K. H., Kang H. K., Wong C. C., Zong Y. and Knoll W., Azimuthal dispersion and energy mode condensation of grating-coupled surface plasmon polaritons, *Phys. Rev. B* 77, 245435-245441 (2008).

[17] Romanato F., Lee K. H., Kang H. K., Ruffato G. and Wong C. C., Sensitivity enhancement in grating coupled surface plasmon resonance by azimuthal control, *Opt. Express* 17, 12145-12154 (2009).

[18] Romanato F., Lee K. H., Ruffato G. and Wong C. C., The role of polarization on surface plasmon polariton excitation on metallic gratings in the conical mounting, *Appl. Phys. Lett.* 96, 111103 (2010).

[19] Maldovan M., Thomas E. L., Periodic Materials and Interference Lithography. Wiley-VCH Verlag GmbH & Co. KGaA, 2008.

[20] Zacco G., Romanato F., Sonato A., Sammito D., Ruffato G., Morpurgo M., Silvestri D., Carli M., Schiavuta P. and Brusatin G., Sinusoidal plasmonic crystals for bio-detection sensors, *Microelectron. Eng.* 88, 1898-1901 (2011).

[21] Cabral J. T., Hudson S. D., Harrison C., and Douglas J. F., Frontal Photopolymerization for Microfluidic Applications, *Langmuir* 20, 10020-10029 (2004).

[22] Technical data sheet for NOA optical adhesives; Norland Products, Inc.: New Brunswick, NJ.

[23] Chandezon J., Maystre D. and Raoult G., A new theoretical method for diffraction gratings and its numerical application, *J. Optics (Paris)* 11, No. 4, 235-241 (1980).

[24] Chandezon J., Dupuis M. T. and Cornet G., Multicoated gratings: a differential formalism applicable in the entire optical region, *J. Opt. Soc. Am.* 72, No. 7, 839-846 (1982).

[25] Elston S. J., Bryan-Brown G. P. and Sambles J. R., Polarization conversion from diffraction gratings, *Phys. Rev. B* 44, No.12, 6393-6400 (1991).

[26] Granet G., Plumey J. P. and Chandezon J., Scattering by a periodically corrugated dielectric layer with non identical faces, *Pure Appl. Opt.* 4, No.1, 1-5 (1995).

[27] Preist T. W., Cotter N. P. K. and Sambles J. R., Periodic multilayer gratings of arbitrary shape, *J. Opt. Soc. Am. A* 12, No. 8, 1740-1749 (1995).

[28] Li L., Granet G., Plumey J. P. and Chandezon J., Some topics in extending the C-method to multilayer-coated gratings of different profiles, *Pure Appl. Opt.* 5, No.2, 141-156 (1996).

[29] Plumey J. P., Guizal B. and Candezon J., Coordinate transformation method as applied to asymmetric gratings with vertical facets, *J. Opt. Soc. Am. A* 14, No. 3, 610-617 (1997).

[30] Li L., Multilayer-coated diffraction gratings: differential method of Chandezon et al. revisited, *J. Opt. Soc. Am. A* 11, 2816-2828 (1994).

[31] Li L., Using symmetries of grating groove profiles to reduce computation cost of the C-method, *J. Opt. Soc. Am. A* 24, 1085-1096 (2007).

[32] Post E. J., Formal Structure of Electromagnetics. North-Holland, Amsterdam, 1962.

[33] Ashcroft N. W. and Mermin N. D., Solid State Physics. Saunders College Publishing, 1976.

[34] Zygmund A., Trigonometric Series. Cambridge U. Press, Cambridge, 1977.

[35] Li L., Use of Fourier series in the analysis of discontinuous periodic structures, *J. Opt. Soc. Am. A* 13, No. 9 (1996).

[36] Li L., Justification of matrix truncation in the modal methods of diffraction gratings, *J. Opt. A: Pure Appl. Opt.* 1, 531-536 (1999).

[37] Ruffato G., Zacco G. and Romanato F., Surface Plasmon Polaritons Excitation and Propagation on Metallic Gratings: Far-Field and Near-Field Numerical Simulations, *Journal of Materials Science and Engineering A* 1, No. 6, 768-777 (2011).

[38] Dorsey E., Properties of Ordinary Water-Substance, Reinhold Publishing Corporation 1940.

[39] Ruffato G. and Romanato F., Grating-Coupled Surface Plasmon Resonance in conical mounting with Polarization Modulation, *Opt. Lett.* 37 (2012).

[40] Ang X. F., Li F. Y., Tan W. L., Chen Z. and Wong C. C., Self-assembled monolayer for reduced temperature direct metal thermocompression bonding, *Appl. Phys. Lett.* 91, 061913 (2007).

[41] Johansen K., Stalberg R., Lundstrom I., Liedberg B., Surface plasmon resonance: instrumental resolution using photo diode arrays, *Meas. Sci. Technol.* 11, 1630-1638 (2000).

[42] Jung L. S., Campbell C. T., Chinowsky T. M., Mar M. N. and Yee S. S., Quantitative interpretation of the response of surface plasmon resonance sensors to adsorbed films, *Langmuir* 14, 5636-5648 (1998).

[43] Bain C. D., Troughton E. B., Tao Y. T., Evall J., Whitesides G. M., Nuzzo R. G., Formation of monolayer films by the spontaneous assembly organic thiols from solution onto gold, *J. Am. Chem. Soc.* 111, 321-335 (1989).